nature synthesis

Article

https://doi.org/10.1038/s44160-026-01115-3

Assembly of a bifurcated knot via sequence selective imine condensation

Received: 28 January 2026

Accepted: 11 June 2026

Published online: 16 July 2026

Check for updates

James T. F. Dobson[1,5], Jack A. Davies[1,5], Tanya K. Ronson[1], Andrew Tarzia[2,3,4], Xiang Sun[1], Kim E. Jelfs[3] & Jonathan R. Nitschke[1]

Knotting and weaving, at both macroscopic and molecular scales, play an essential role in determining the physical properties of materials. While classical crossing points in molecular knots have been extensively studied, synthetic bifurcated knots, containing characteristic junctions where a strand divides into two branches, represent an underexplored class of topologically complex molecular knots. Although reports of such structures are rare due to synthetic challenges, natural bifurcated knots have been identified in proteins and linked to potentially enhancing protein robustness. Here we report the synthesis of a 524-atom bifurcated knot featuring 3 classical crossings and 20 bifurcated junctions via 2 sequential, selective, imine condensations. First, Zn^{II} ions are used to template the subcomponent self-assembly of a $Zn^{II}_8L_6$ architecture, with three unreacted aldehyde groups protruding from each of its eight vertices. Second, a geometry-matching tris-aniline condenses with these terminal aldehydes, yielding a covalently linked bifurcated knot with enhanced robustness, as quantified using collision-induced dissociation mass spectrometry. We anticipate that this approach will facilitate the design of new mechanically interlocked molecules and highly entangled molecular materials with increased robustness.

Inspired by naturally occurring knotted biomolecules, such as DNA and proteins[1,2], as well as macroscopic woven materials, synthetic molecular knots have been pursued for their topological complexity and potential functionality[3–6]. Their targeted synthesis has been enabled by a range of strategies, typically involving the assembly of a preorganized scaffold followed by the closure of functionalized molecular strand termini. Notable methods[7] include metal-templated self-assembly[8–11] and hydrogen bonding[12], which are often used to assemble grid architectures[13] and cyclic helicate scaffolds[11]. Subsequent strand tying is commonly achieved through ring-closing olefin metathesis[10,14], Glaser couplings[15,16] or other covalent linkages[9], granting access to an expanding family of molecular knots, including trefoils[8], pentafoils[11], 7_4 knots[13], 8_{19} knots[9,17] and even 12 crossing knots[18].

Beyond their intellectual appeal on the grounds of synthetic challenge, molecular knots have demonstrated functional use in catalysis[3,19], guest binding[20] and therapeutics[21]. Analogous to the impact of entanglements in woven macroscopic materials and polymers, their presence in molecular materials has also been shown to influence elasticity and tensile strength[22–24]. On the contrary, bifurcations, defined as points where a strand divides into two branches, constitute an underexplored feature in knotted molecular materials and reports of architectures that contain both classical crossing points and bifurcated junctions are scarce[25–27]. Nonetheless, bifurcated junctions, or branching points, are known to play a key role in determining the physical properties, such as elasticity, of molecular materials including polymers[28] and DNA nanostar hydrogels[29]. More recently, bifurcated knots have been found to occur naturally in proteins when disulfide and ionic bonds form internal bridges between non-consecutive amino acids, introducing bifurcations and generating so called θ-curves[30]. Non-trivial (knotted) θ-curves formed through ionic bonds may play

[1]Yusuf Hamied Department of Chemistry, University of Cambridge, Cambridge, UK. [2]School of Chemistry, University of Birmingham, Birmingham, UK. [3]Department of Chemistry, Molecular Sciences Research Hub, Imperial College London, London, UK. [4]Department of Applied Science and Technology, Politecnico di Torino, Torino, Italy. [5]These authors contributed equally: James T. F. Dobson, Jack A. Davies. e-mail: jrn34@cam.ac.uk

a role in protein active sites, whereas those formed through disulfide bonds could be important for protein stabilization[30]. Thus, the development of new synthetic tools to access knotted architectures containing bifurcations will unlock new routes towards designing topologically complex molecules with increased robustness.

In this work, we report the subcomponent self-assembly of bifurcated knot **3**. Three different organic subcomponents assembled together around Zn^{II} ions to form **3**, with each subcomponent bringing specific properties that allow for the synthesis of the desired knot in a two-step process. In the first step, the mismatch in lengths along the two sides in rectangular subcomponent **A** precludes the formation of a pseudo-cubic architecture and instead directs the assembly of $Zn^{II}_8L_6$ framework **2**. Architecture **2** can be considered as a $Zn^{II}_2L_3$ helicate threaded through a $Zn^{II}_6L_3$ triangular prism, where the 8 Zn^{II} ions reside at the vertices of a distorted elongated triangular bipyramid (the 14th Johnson solid[31], J_{14}). The difunctional subcomponent **B** used in the assembly of **2** was designed to favour initial imine condensation at the 2-position, leaving the aldehyde at the 5-position extending away from the vertex. This selective functionalization creates termini that may be subsequently linked together in a second step. Tris-aniline **C** was introduced in the presence of the strong acid bis(trifluoromethane)sulfonimide ($HNTf_2$) to protonate the tertiary amine at the core of the subcomponent. We infer this protonation to result in its hydrogen-bonding-driven preorganization into a bowl-like conformation, optimal for capping cage vertices[32]. The acid may also play two further roles: catalysing imine bond formation at the vertex, and mitigating the risk of Zn^{II} extraction from architecture **2** through protonation of the tertiary amine in **C**. This second step transforms the structure into a closed organic strand woven around eight templating metal centres, providing an 89% yield of molecular knot **3**, which integrates eight additional bifurcations.

$Zn^{II}_8L_6$ framework 1

The framework for the knot described herein, without the uncondensed aldehyde groups extending from each vertex, emerged during investigations into the self-assembly behaviour of rectangular tetrakis-anilines. The subcomponent **A** assembled with 2-formylpyridine and zinc(II) bis(trifluoromethanesulfonyl)imide (triflimide, $^{-}NTf_2$) in acetonitrile to yield metal-organic architecture **1** (Fig. 1).

Single crystals of **1** suitable for X-ray diffraction (XRD) analysis were grown by vapour diffusion of benzene into a nitromethane solution of $\mathbf{1}\cdot(NTf_2)_{16}$ containing excess $^{n}Bu_4\cdot ClO_4$ (^{n}Bu = *n*-butyl). The solid-state structure was solved by single-crystal XRD at the Diamond Light Source Synchrotron, revealing a $[Zn^{II}_8L_6]^{16+}$ metal-organic architecture (Supplementary Fig. 66), where the 8 Zn^{II} centres occupy the vertices of a distorted elongated triangular bipyramid, the 14th Johnson solid[31] (J_{14}) (Fig. 1c).

Six of the eight *fac* Zn^{II} centres have the same handedness, describing a distorted triangular prism. In Fig. 1, these Zn^{II} centres have Δ handedness and are coloured orange. Three $\mathbf{L^A}$ units, which form by the condensation of tetrakis-aniline **A** with four equivalents of 2-formylpyridine, define the three quadrilateral faces of the $Zn^{II}_6L_3$ distorted triangular prism and are shown in blue. The remaining two Zn^{II} vertices exhibit the opposite handedness to the six Zn^{II} centres describing the prism and are coloured purple. These two Zn^{II} centres are bridged by the long axes of three additional $\mathbf{L^A}$ ligands (coloured grey), forming an inner $Zn^{II}_2L_3$ helicate. The remaining pyridyl-imine binding sites on the three helicate-forming ligands chelate Zn^{II} centres within the outer $Zn^{II}_6L_3$ distorted triangular prism. All eight Zn^{II} centres within **1** are thus chelated by three pyridyl-imine ligands and have pseudo-octahedral coordination geometries.

The signals in the high-resolution mass spectrometry (HRMS) of **1** (Fig. 1b and Supplementary Figs. 30 and 31) correspond well to the expected ones for a $Zn^{II}_8L_6\cdot(NTf_2)_{16}$ architecture. The ^{1}H NMR spectrum (Fig. 1b and Supplementary Figs. 20 and 21) of **1** contains up to four times the number of signals expected for the free ligand, assuming free rotation about C–C bonds, indicating the presence of four magnetically distinct ligand arm environments within **1**. The HRMS and ^{1}H NMR spectroscopy data for **1** are thus consistent with the X-ray crystal structure, where each of the two distinct ligand environments, coloured differently in Fig. 1, contains two distinct types of ligand arm.

In previously reported $Zn^{II}_8L_6$ pseudo-cubic architectures, the short and long axes of rectangular tetrakis-aniline subcomponents must converge at the same edges of the polyhedron, generating mismatches[33]. X-ray crystallographic analysis of **1** revealed that no such mismatched edges were present. The mean N···N distance between imine nitrogens along the long axis of **A** is 20.6 ± 0.3 Å, whereas along the short axis it is 12.1 ± 0.1 Å. Although there are two distinct ligand environments—the outer faces of a distorted triangular prism and the inner strands of a triple helicate—the small standard deviations for the values of N···N distances indicate that the ligands arrange themselves within **1** so as to minimize N···N distance differentials. We infer that the magnitude of the difference in N···N distances between the long and short axes of subcomponent **A** within **1** precludes the incorporation of mismatches between these different axes at polyhedron edges, thereby preventing pseudo-cube assembly. Such pseudo-cubes would incorporate too much strain.

The preference for structure **1** to exhibit the geometry observed may stem from the absolute difference in N···N separations along distinct axes of **A**. A smaller Δ(N···N) would make the centre of the $Zn^{II}_6L_3$ triangular prism subunit too narrow to accommodate the $Zn^{II}_2L_3$ helicate core. By contrast, a larger Δ(N···N) could render the $Zn^{II}_6L_3$ prism too wide for the short axis of tetrakis-aniline **A** to bridge between a Zn^{II} centre in the helicate and a Zn^{II} centre in the prism.

Rotatable C–C bonds in the tetraphenyl backbone of tetrakis-aniline **A** imbue the resulting $\mathbf{L^A}$ ligands with conformational flexibility relating to the twist along their long axis. The ligands panelling the three quadrilateral faces of the $Zn^{II}_6L_3$ triangular prismatic subunit exhibited a mean twist of 25 ± 6° (Fig. 1d, left), calculated as the dihedral angle shown in Fig. 1d. The ligands that form the $Zn^{II}_2L_3$ helicate subunit have a much greater twist of 73 ± 5° (Fig. 1d, right). We thus infer the ability of the ligand to adopt conformations with differing degrees of twist to play a crucial role in directing the assembly of structure **1**.

To further investigate the structural preference observed in **1**, computational models of isostructural architectures were generated for a series of rectangular tetrakis-anilines using an automated, high-throughput structure generation workflow[33] (Supplementary Section 4). These structures were constructed with stk[34] and geometry-optimized through a workflow involving UFF4MOF[35–37] in GULP[38,39] and finally GFN2-xTB[40,41]. Using this approach, for a given tetratopic building block, the relative strains were evaluated between different isomers of pseudo-cubes versus the structure type observed for architecture **1** (Supplementary Fig. 72 and Table 4). Notably, for subcomponent **A**, architecture **1** emerged as the lowest-energy structure. The structure of **1** generated computationally showed excellent agreement with the crystal structure (Supplementary Fig. 69). For the other tetratopic subcomponents examined computationally, pseudo-cubic architectures were more energetically favourable than the corresponding structure **1** analogues, as has been observed experimentally[33].

Preparation of a bifurcated knot

The $Zn^{II}_8L_6$ scaffold in architecture **1** is a bifurcated metalla-knot, where the metal ions form part of the knotted strand. Several elegant metalla-knots have been reported[42–45], but their design does not provide a pathway for their conversion into wholly organic strands. The strategy developed here and outlined in detail below allows for the topology of the parent metalla-knot to be conserved as a wholly organic strand. This method could enable the conversion of a variety of entangled metallo-supramolecular structures into fully organic analogues.

Examination of the crystal structure revealed that tying together the three ligand arms coordinating the same metal centre at each of

https://doi.org/10.1038/s44160-026-01115-3

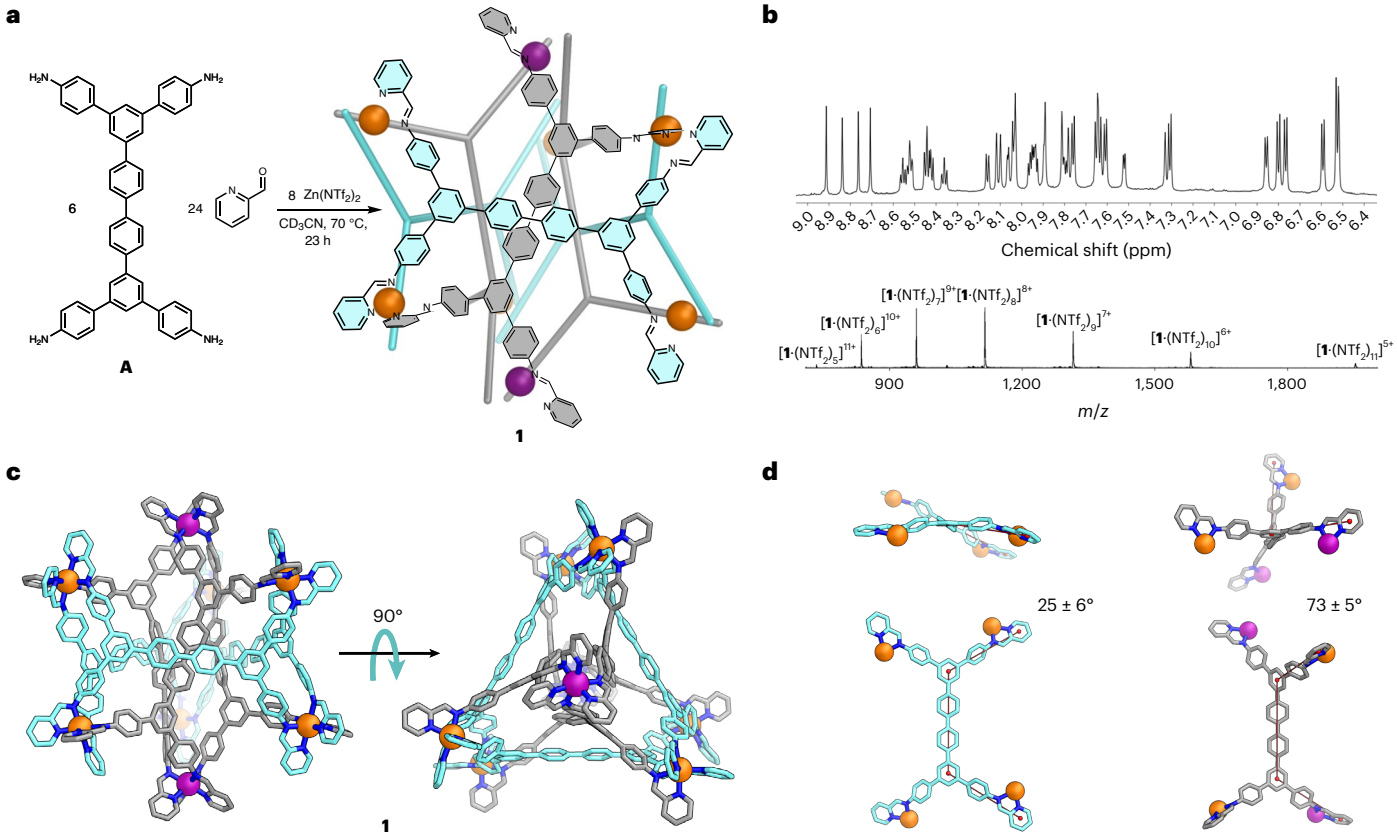


Fig. 1 | Synthesis and characterization of structure 1, including its single-crystal structure and variable ligand twist angle measurements. **a**, Subcomponent self-assembly of metal-organic architecture **1**. The schematic depiction of **1** is based on its X-ray crystal structure. **b**, Partial ^{1}H NMR (700 MHz, CD_3CN, 298 K) and HRMS spectra of **1**. **c**, Two views of the X-ray crystal structure of metal-organic architecture **1**. Solvent, counterions, disorder and hydrogen atoms are omitted for clarity. **d**, Ligands integrated into the $Zn^{II}_6L_3$ triangular prism subunit (left) and the $Zn^{II}_2L_3$ helicate subunit (right), respectively, extracted from the X-ray crystal structure of **1**. The twists in the ligands are described by the mean dihedral angles indicated. Errors correspond to the standard deviations between crystallographically distinct ligands. Zn^{II}, orange (*fac*-Δ stereochemistry) and purple (*fac*-Λ stereochemistry); N, blue; C, light blue or grey, coloured depending on the ligand environment.

the eight vertices in structure **1** would yield a topologically intricate bifurcated knot. This structure incorporates an unprecedented 20 bifurcated junctions alongside three classical crossing points in a new topology. However, past methods that have enabled tying functionalized molecular strand termini together, which have been successfully used in the synthesis of other knotted molecules[10,15,16], were unsuitable here. For example, olefin metathesis can tie two strands together[10], whereas the formation of this structure required the simultaneous tying of three molecular strands.

Dynamic imine chemistry has been used for the one-pot synthesis of molecular knots[46–48] and for the conversion of preformed scaffolds into interlocked organic molecules via imine exchange, which generally involves the replacement of a monotopic amine with a multitopic (often ditopic) amine[9,49]. Using analogous one-pot and imine exchange strategies to yield structure **1** as a wholly organic strand would require the use of a tritopic 2-formylpyridine-based subcomponent. The challenge of designing and synthesizing a tris-2-formylpyridine subcomponent with a suitable geometry and flexibility to cap the vertices of structure **1** would present a challenge for both approaches. Furthermore, in the case of a one-pot strategy involving the combination of tetrakis-aniline **A** and a tris-2-formylpyridine subcomponent, selectively forming a discrete structure over polymeric species may pose a further challenge. For imine exchange, the replacement of individual 2-formylpyridine units with the multitopic 2-formylpyridine derived subcomponent would be required in the present case. However, imine exchange involving the replacement of one 2-formylpyridine for another has proved more challenging to control for subcomponent self-assembled metal-organic architectures[50] than the exchange of one amine residue for another, as it involves greater structural disruption.

We thus devised a two-step synthetic strategy to access the desired bifurcated knot (Fig. 2), distinct from extensions of the one-pot and imine exchange methods discussed above. In the first step, dialdehyde subcomponent **B** was incorporated in place of 2-formylpyridine, enabling the assembly of an aldehyde-functionalized analogue of architecture **1**. We proposed that the asymmetry of subcomponent **B** would drive selective imine bond formation at the carbonyl adjacent to the pyridine nitrogen as a result of metal templation and the enhanced electrophilicity bestowed by proximity to the pyridine nitrogen. The aldehyde at the 5-position would thus remain unreacted, facilitating vertex-capping in the second step by a triamine. This vertex-capping would result in the desired tying together of the three ligands converging at the same Zn^{II} cation, yielding a wholly organic structure containing the targeted 20 bifurcated junctions and three classical crossing points. Eight of the bifurcated junctions in the organic strand are installed during the vertex-capping step, while the other 12 bifurcated junctions in the organic strand and 3 crossing points were already present within the metalla-knot.

The subcomponent self-assembly of tetrakis-aniline **A**, pyridine-2,5-dicarbaldehyde (**B**) and $Zn(NTf_2)_2$ yielded metal-organic architecture **2**. NMR spectra (Fig. 2b and Supplementary Figs. 32, 33 and 37) and HRMS data (Supplementary Figs. 42 and 43) indicated that **2** was isostructural to **1**, with three additional uncondensed aldehydes

https://doi.org/10.1038/s44160-026-01115-3

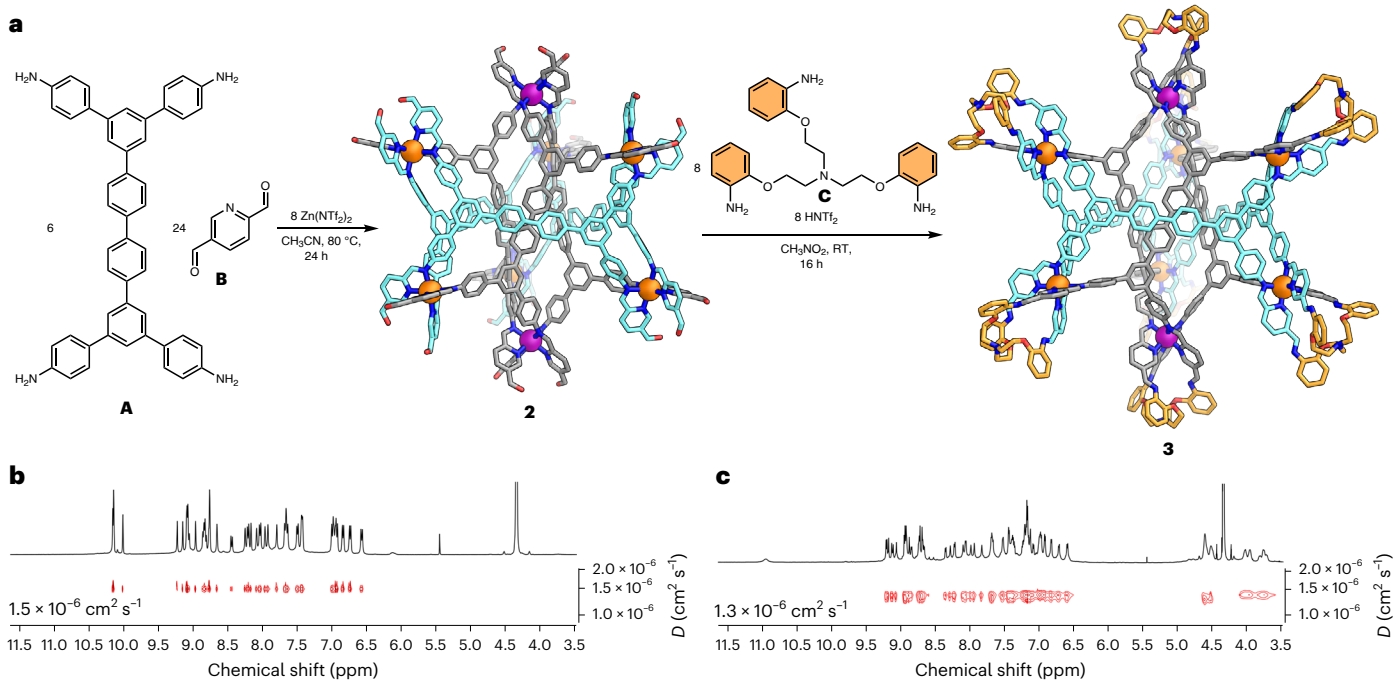


Fig. 2 | Synthesis and characterization of architectures 2 and 3. a, Synthetic route to structures **2** and **3**; the atom colouring is the same as in Fig. 1, with the addition of **C**: orange for the caps. The MM3 models of structures **2** and **3** were constructed from the crystal structure of architecture **1**. **b**, ^{1}H NMR and diffusion-ordered spectra (400 MHz, CD_3NO_2, 298 K) of architecture **2**. **c**, ^{1}H NMR and diffusion-ordered spectra (400 MHz, CD_3NO_2, 298 K) of bifurcated knot **3**. RT, room temperature.

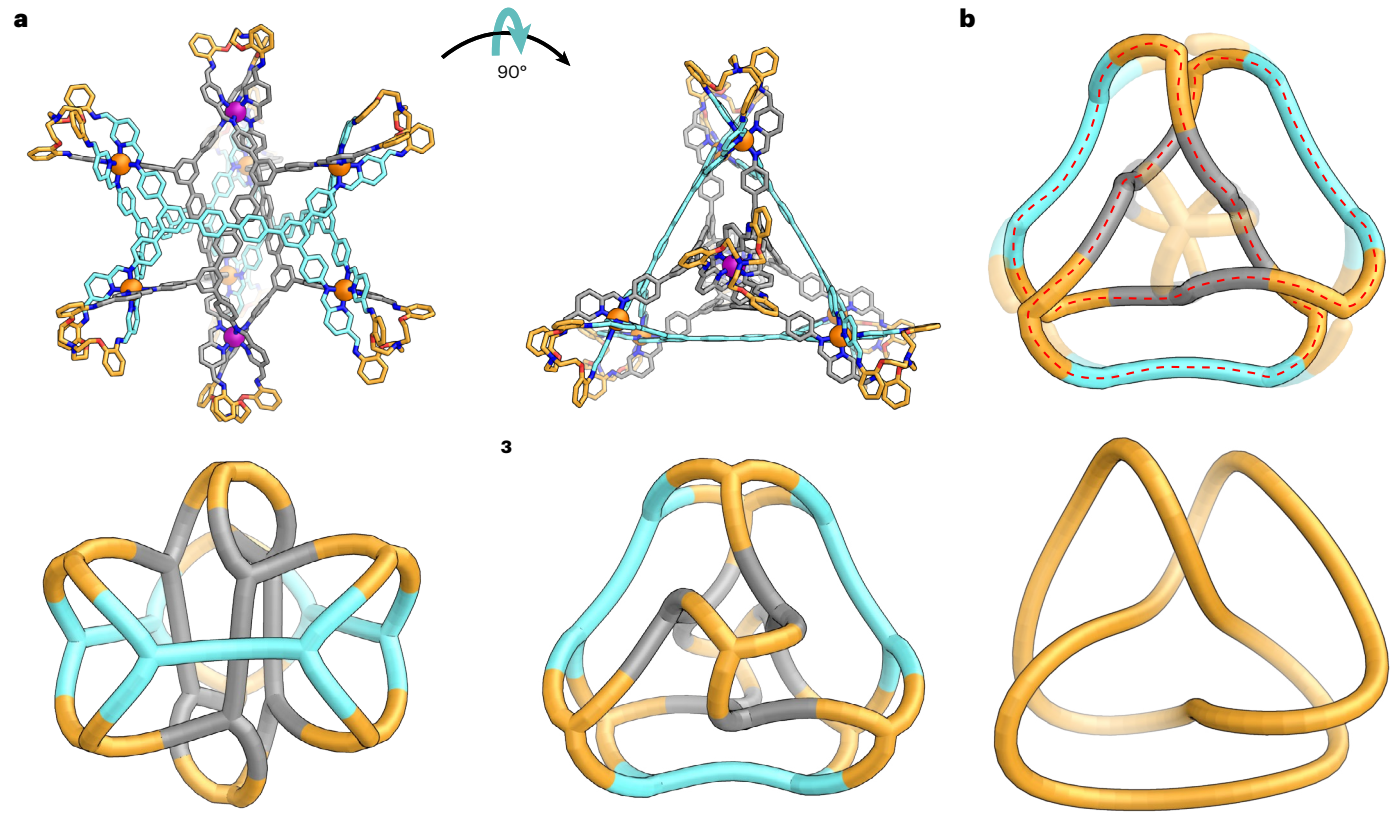


Fig. 3 | Cartoon representation of bifurcated knot 3 and tracing of the 3_1-trefoil knot motif within. a, Top: MM3 model of **3** based on the crystal structure of **1**. Bottom: cartoon representations of its bifurcated knot topology, with the shortest continuous path length of 524 atoms, as seen down the C_2 (left) and C_3 (right) axes. **b**, Top: the dashed red path illustrates the 3_1-trefoil knot present within **3**, with additional branches shown as faded strands. Bottom: cartoon model of a 3_1-trefoil knot.

https://doi.org/10.1038/s44160-026-01115-3

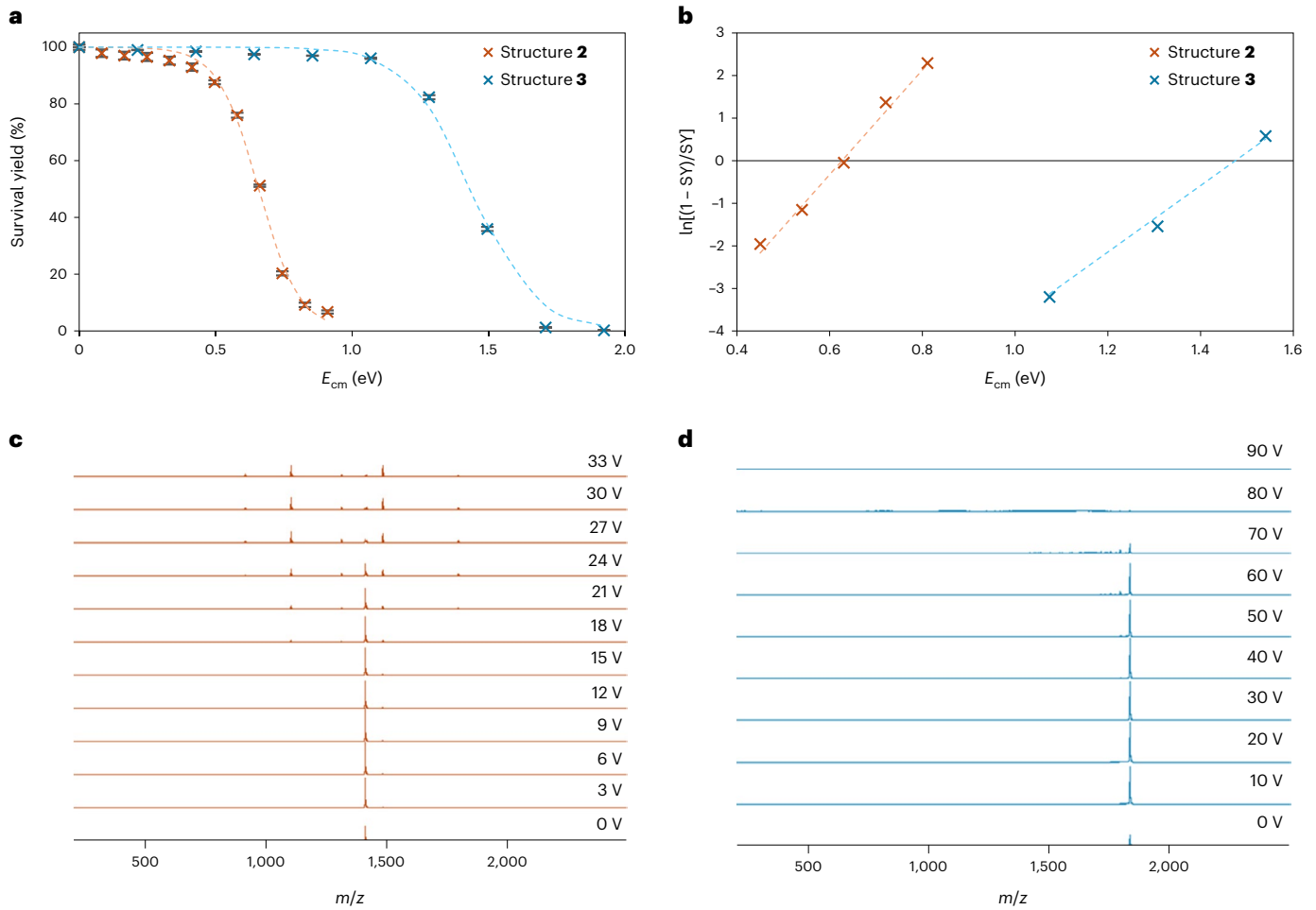


Fig. 4 | Breakdown curves for structures 2 and 3 and their respective gMS² spectra. a, gMS² experiments were conducted to afford breakdown curves for structures **2** and **3** (Supplementary Section 5). Survival yield (SY; %) is plotted as a function of the centre-of-mass collision energy (E_{cm}; eV). For each fragmentation curve, three runs were conducted, with the mean values plotted ($n = 3$ independent experiments). Error bars correspond to the standard deviations between runs. **b**, Linearizing the breakdown curves in **a** affords plots where the x intercept corresponds to the energy required for 50% dissociation (CE_{50}) of the parent ion. **c**, gMS² spectra for structure **2**. **d**, gMS² spectra for structure **3**.

protruding from each of the eight Zn^{II} vertices. The subsequent addition of triamine **C** to **2**, in the presence of 1.5 equivalents of $HNTf_2$ per triamine, yielded bifurcated knot **3**. Notably, attempts to perform this transformation in the absence or with substoichiometric amounts of acid failed to yield **3** (Supplementary Fig. 59).

^{1}H NMR spectroscopy (Fig. 2c and Supplementary Figs. 44 and 45) revealed the disappearance of the four signals characteristic of the aldehyde environments in **2**, alongside the emergence of four new signals for the imines of **3** (Supplementary Fig. 49), indicating the retention of symmetry. HRMS signals (Supplementary Figs. 55 and 57) also were in excellent agreement with the expected isotopic patterns for **3**.

Our approach proceeded with high yield (roughly 90%) and directly incorporated bifurcations into the final structure, thus complementing and building on previous methods for tying molecular strands[10,15,16].

From a topological perspective, the shortest continuous path around bifurcated knot **3** (Fig. 3a) consists of a closed loop of 524 atoms woven around 8 templating Zn^{II} ions, featuring 3 crossing points and 20 bifurcated junctions. Structurally, **3** can be viewed as a 3_1-trefoil knot with additional branches, as illustrated in Fig. 3.

Gas-phase quantification of stability

Our capping strategy covalently ties three ligand arms together at each vertex. To quantify the degree to which this structural modification stabilizes the resulting architecture, gradient tandem mass spectrometry (gMS²) experiments (Fig. 4c,d) were run to determine the collision energies required to dissociate bifurcated metalla-knot **2** and covalently linked bifurcated knot **3**[51]. The 7+ peaks for each complex were selected and isolated within the quadrupole. These ions were then exposed to increasingly higher voltages in the trap cell, resulting in decomposition through collision-induced dissociation with residual argon gas. A 50% reduction in signal intensity for **2** was found to occur at 23.9 ± 0.095 V, corresponding to a centre-of-mass collision energy of 0.660 ± 0.003 eV (Fig. 4a,b). By contrast, structure **3** did not reach a 50% reduction in intensity until a trap voltage was applied of 67.500 ± 0.276 V, corresponding to a centre-of-mass collision energy of 1.440 ± 0.006 eV.

For **3**, the combination of both dynamic-covalent imine bonds and Zn^{II} coordination holds the structure together, as opposed to only Zn^{II} coordination in **2**. This difference results in more than twice as much energy being required to dissociate **3** than **2**. These collision-induced dissociation measurements thus indicate that covalent capping translated the topological complexity of **3** into greater robustness.

Extending Alexander–Briggs notation

We anticipate that more highly entangled bifurcated structures will be reported in the coming years, as the methods introduced herein and other recent synthetic developments[25,26] find greater use. This class of materials thus needs a standardized nomenclature to classify these

structures and identify their topological characteristics. Here we propose an extension of the Alexander–Briggs notation[52] that allows for a description of topological complexity extending beyond the number of crossing points by including a term that summarizes the total number of junctions (J) in the structure, and their degree of branching (m):

$$(C_n, J_{m,x}) \quad (1)$$

In this notation, C is the number of classical crossings, n the number in the series, J the number of junctions, m the degree of branching (for example, bifurcation is 2, and trifurcation is 3) and x the order in the series. C_n denotes the highest-order knot that can be traced within the overall topology without repeating paths or junctions. Figure 3b shows that a 3_1-trefoil knot can be traced through bifurcated knot **3**; thus C_n is 3_1 for structure **3**.

For structure **3**, the notation reads (3_1, $20_{2,1}$). This notation is intended to facilitate direct structural comparisons between different classes of highly entangled materials, such as perplexanes[26], trefoil tetrahedra[25] and other knotted molecules containing junctions[53,54]. For a more detailed discussion of this notation and examples of its implementation to structures in the literature, see Supplementary Section 6.

Conclusion

A large enough edge-length mismatch in tetrakis-aniline subcomponent **A** thus precludes the assembly of a pseudo-cubic architecture, instead directing assembly of $Zn^{II}_8L_6$ structure **2** with a distinct geometry, comprising a triple helicate threaded through the centre of a triangular prism. The terminal aldehydes extending from the vertices of architecture **2** facilitate vertex-capping with a geometrically compatible tris-aniline, ultimately yielding a bifurcated knot (**3**). This two-step strategy establishes a synthetic approach for simultaneously tying three molecular strand termini, thus granting access to a previously inaccessible topology. Many distinct types of metal-organic architecture have been reported using the combination of multitopic amine-based and monotopic 2-formylpyridine-based subcomponents, with many more possible. The ability to convert such metal-organic architectures into wholly organic analogues allows for the synthesis of molecules with substantially enhanced robustness. Furthermore, the ability to introduce organic bifurcated junctions within a knotted framework will allow for the synthesis of more complex entangled molecules and materials.

Methods

Self-assembly of 1

To a mixture of tetrakis-aniline **A** (5.1 mg, 7.6 µmol, 1.0 equiv.) and $Zn(NTf_2)_2$ (6.9 mg, 11 µmol, 1.4 equiv.) in deuterated acetonitrile (0.6 ml), 2-formylpyridine (3.0 µl, 32 µmol, 4.1 equiv.) was added. The reaction mixture was heated at 70 °C for 23 h. The reaction mixture was allowed to cool to room temperature, filtered through a glass fibre filter paper plug and concentrated to a small volume. Diethyl ether (8 ml) was added to induce precipitation. The solid was washed with diethyl ether (3 × 8 ml) and the product **1**·$(NTf_2)_{16}$ was obtained as a yellow-orange solid (12.6 mg, 1.10 µmol, 85%).

Self-assembly of 2

To a solution of subcomponent **B** (13.7 mg, 101 µmol, 4.50 equiv.) and $Zn(NTf_2)_2$ (20.6 mg, 32.9 µmol, 1.50 equiv.) in CH_3CN (3.80 ml), a suspension of subcomponent **A** (15.1 mg, 22.5 µmol, 1.00 equiv.) in CH_3CN (3.80 ml) was added dropwise at room temperature with vigorous stirring. The reaction mixture was heated at 80 °C for 24 h. The solution was allowed to cool to room temperature, filtered through glass fibre filter paper and concentrated (to roughly 3–4 ml) using a stream of N_2(g). Et_2O (roughly 10 ml) was added, and the orange precipitate was collected by centrifugation. The precipitate was washed with Et_2O (3 × 10 ml) and **2**·$(NTf_2)_{16}$ was obtained as an orange solid (31.7 mg, 2.68 µmol, 71%).

Self-assembly of 3

To a solution of structure **2** (21.5 mg, 1.82 µmol, 1.00 equiv.) in CH_3NO_2 (2 ml), a premixed solution of **C** (7.35 mg, 17.4 µmol, 9.60 equiv.) and $HNTf_2$ (7.34 mg, 26.1 µmol, 14.4 equiv.) in CH_3NO_2 (1 ml) was added dropwise with vigorous stirring at room temperature. The mixture was stirred for 16 h under ambient conditions, filtered through glass fibre filter paper and Et_2O (roughly 5 ml) was added. The precipitate was separated by centrifugation and washed with Et_2O (10 ml), 10% CH_3NO_2:Et_2O (10 ml) and Et_2O (10 ml). **3**·$(NTf_2)_{16}$·$(HNTf_2)_8$ was obtained as an orange solid (27.5 mg, 1.61 µmol, 89%).

Data availability

Data for this paper, including structure files and properties, are available via Zenodo at https://doi.org/10.5281/zenodo.17589446 (ref. 55). Crystallographic data for the structures reported in this paper have been deposited at the Cambridge Crystallographic Data Centre (CCDC), under the deposition numbers 2497146 (architecture **1**) and 2536280 (architecture **5**). Copies of these data can be obtained free of charge via www.ccdc.cam.ac.uk/data_request/cif. Source data are provided with this paper.

Code availability

The code used to generate the structures is available via GitHub at https://github.com/andrewtarzia/sca_cage_assembler/tree/spindles-production and via Zenodo at https://doi.org/10.5281/zenodo.17999611 (ref. 56).

References

1. Sułkowska, J. I., Rawdon, E. J., Millett, K. C., Onuchic, J. N. & Stasiak, A. Conservation of complex knotting and slipknotting patterns in proteins. *Proc. Natl Acad. Sci.* **109**, 1715–E1723 (2012).
2. Liu, L. F., Liu, C. C. & Alberts, B. M. Type II DNA topoisomerases: enzymes that can unknot a topologically knotted DNA molecule via a reversible double-strand break. *Cell* **19**, 697–707 (1980).
3. Marcos, V. et al. Allosteric initiation and regulation of catalysis with a molecular knot. *Science* **352**, 1555–1559 (2016).
4. Hu, Y. et al. Transmembrane ion channels formed by a Star of David [2]catenane and a molecular pentafoil knot. *J. Am. Chem. Soc.* **142**, 18859–18865 (2020).
5. Fielden, S. D. P., Leigh, D. A. & Woltering, S. L. Molecular knots. *Angew. Chem. Int. Ed.* **56**, 11166–11194 (2017).
6. Ashbridge, Z. et al. Knotting matters: orderly molecular entanglements. *Chem. Soc. Rev.* **51**, 7779–7809 (2022).
7. Ayme, J. F., Beves, J. E., Campbell, C. J. & Leigh, D. A. Template synthesis of molecular knots. *Chem. Soc. Rev.* **42**, 1700–1712 (2013).
8. Dietrich-Buchecker, C. O. & Sauvage, J.-P. A synthetic molecular trefoil knot. *Angew. Chem. Int. Ed.* **28**, 189–192 (1989).
9. Carpenter, J. P. et al. Controlling the shape and chirality of an eight-crossing molecular knot. *Chem* **7**, 1534–1543 (2021).
10. Zhang, L. et al. Stereoselective synthesis of a composite knot with nine crossings. *Nat. Chem.* **10**, 1083–1088 (2018).
11. Ayme, J. F. et al. A synthetic molecular pentafoil knot. *Nat. Chem.* **4**, 15–20 (2011).
12. Feigel, M., Ladberg, R., Engels, S., Herbst-Irmer, R. & Fröhlich, R. A trefoil knot made of amino acids and steroids. *Angew. Chem. Int. Ed.* **45**, 5698–5702 (2006).
13. Leigh, D. A. et al. A molecular endless (74) knot. *Nat. Chem.* **13**, 117–122 (2020).
14. Du, C., Padgham, A. C., Slater, A. G. & Zhang, L. Efficient flow synthesis of a Star of David [2]catenane and a pentafoil knot. *Chem* **11**, 102328 (2025).
15. Carina, R. F., Dietrich-Buchecker, C. & Sauvage, J. P. Molecular composite knots. *J. Am. Chem. Soc.* **118**, 9110–9116 (1996).

16. Dietrich-Buchecker, C. O., Khemiss, A. & Sauvage, J. P. High-yield synthesis of multiring copper(I) catenates by acetylenic oxidative coupling. *J. Chem. Soc. Chem. Commun.* **22**, 1376–1378 (1986).
17. Danon, J. J. et al. Braiding a molecular knot with eight crossings. *Science* **355**, 159–162 (2017).
18. Ashbridge, Z. et al. Vernier template synthesis of molecular knots. *Science* **375**, 1035–1041 (2022).
19. Gil-Ramírez, G. et al. Tying a molecular overhand knot of single handedness and asymmetric catalysis with the corresponding pseudo-D3-symmetric trefoil knot. *J. Am. Chem. Soc.* **138**, 13159–13162 (2016).
20. Ayme, J. F. et al. Strong and selective anion binding within the central cavity of molecular knots and links. *J. Am. Chem. Soc.* **137**, 9812–9815 (2015).
21. Benyettou, F. et al. Potent and selective in vitro and in vivo antiproliferative effects of metal–organic trefoil knots. *Chem. Sci.* **10**, 5884–5892 (2019).
22. August, D. P. et al. Self-assembly of a layered two-dimensional molecularly woven fabric. *Nature* **588**, 429–435 (2020).
23. Zhang, M. et al. Mechanical scission of a knotted polymer. *Nat. Chem.* **16**, 1366–1372 (2024).
24. Pieranski, P., Kasas, S., Dietler, G., Dubochet, J. & Stasiak, A. Localization of breakage points in knotted strings. *New J. Phys.* **3**, 10 (2001).
25. Yang, Y. et al. Synthesis of covalently linked knotted cage frameworks. *Nat. Synth.* **4**, 1270–1277 (2025).
26. Bergman, H. M. et al. Discovery of an interlocked and interwoven molecular topology in nanocarbons via dynamic C–C bond formation. *J. Am. Chem. Soc.* **147**, 19132–19138 (2025).
27. Arias, K. I., Zysman-Colman, E., Loren, J. C., Linden, A. & Siegel, J. S. Synthesis of a D3-symmetric 'trefoil' knotted cyclophane. *Chem. Commun.* **47**, 9588–9590 (2011).
28. He, L. et al. Highly robust supramolecular polymer networks crosslinked by a tiny amount of metallacycles. *Nat. Commun.* **15**, 3050 (2024).
29. Palombo, G., Weir, S., Michieletto, D. & Gutiérrez Fosado, Y. A. Topological linking determines elasticity in limited valence networks. *Nat. Mater.* **24**, 454–461 (2025).
30. Dabrowski-Tumanski, P., Goundaroulis, D., Stasiak, A., Rawdon, E. J. & Sulkowska, J. I. Theta-curves in proteins. *Protein Sci.* **33**, e5133 (2024).
31. Johnson, N. W. Convex polyhedra with regular faces. *Can. J. Math.* **18**, 169–200 (1966).
32. Gruzdev, M. S. et al. Triethanolamine-based protic ionic liquids with various sulfonic acids: synthesis and properties. *J. Mol. Liq.* **242**, 838–844 (2017).
33. Davies, J. A. et al. Tetramine aspect ratio and flexibility determine framework symmetry for Zn8L6 self-assembled structures. *Angew. Chem. Int. Ed.* **62**, e202217987 (2023).
34. Turcani, L., Tarzia, A., Szczypiński, F. T. & Jelfs, K. E. stk: an extendable Python framework for automated molecular and supramolecular structure assembly and discovery. *J. Chem. Phys.* **154**, 214102 (2021).
35. Rappé, A. K., Casewit, C. J., Colwell, K. S., Goddard, W. A. & Skiff, W. M. UFF, a full periodic table force field for molecular mechanics and molecular dynamics simulations. *J. Am. Chem. Soc.* **114**, 10024–10035 (1992).
36. Coupry, D. E., Addicoat, M. A. & Heine, T. Extension of the universal force field for metal-organic frameworks. *J. Chem. Theory Comput.* **12**, 5215–5225 (2016).
37. Addicoat, M. A., Vankova, N., Akter, I. F. & Heine, T. Extension of the universal force field to metal-organic frameworks. *J. Chem. Theory Comput.* **10**, 880–891 (2014).
38. Gale, J. D. GULP: a computer program for the symmetry-adapted simulation of solids. *J. Chem. Soc. Faraday Trans.* **93**, 629–637 (1997).
39. Gale, J. D. & Rohl, A. L. The general utility lattice program (GULP). *Mol. Simul.* **29**, 291–341 (2003).
40. Bannwarth, C., Ehlert, S. & Grimme, S. GFN2-xTB—an accurate and broadly parametrized self-consistent tight-binding quantum chemical method with multipole electrostatics and density-dependent dispersion contributions. *J. Chem. Theory Comput.* **15**, 1652–1671 (2019).
41. Bursch, M., Neugebauer, H. & Grimme, S. Structure optimisation of large transition-metal complexes with extended tight-binding methods. *Angew. Chem. Int. Ed.* **58**, 11078–11087 (2019).
42. Dang, L. L., Gao, X., Lin, Y. J. & Jin, G. X. s-Block metal ions induce structural transformations between figure-eight and double trefoil knots. *Chem. Sci.* **11**, 1226–1232 (2020).
43. Dang, L. L. et al. Coordination-driven self-assembly of a molecular figure-eight knot and other topologically complex architectures. *Nat. Commun.* **10**, 2057 (2019).
44. Hwan Kim, D. et al. Coordination-driven self-assembly of a molecular knot comprising sixteen crossings. *Angew. Chem. Int. Ed.* **57**, 5669–5673 (2018).
45. Jiao, Y. et al. Metal–organic polyhedra containing 36 and 24 folds of amide groups for selective luminescent recognition of natural disaccharides. *Chem. Commun.* **48**, 6022–6024 (2012).
46. Wu, L. et al. Synthesis of contra-helical trefoil knots with mechanically tuneable spin-crossover properties. *Nat. Synth.* **2**, 17–25 (2022).
47. Sarwa, A. et al. The interplay between component denticity and flexibility promotes the formation of [$Ag^{I}\cdots Ag^{I}$]-stabilised links and knots. *Angew. Chem. Int. Ed.* **64**, e202423962 (2025).
48. Sarwa, A. et al. Iminopyrrole-based self-assembly: a route to intrinsically flexible molecular links and knots. *Angew. Chem. Int. Ed.* **63**, e202316489 (2024).
49. Ayme, J. F., Beves, J. E., Campbell, C. J. & Leigh, D. A. Probing the dynamics of the imine-based pentafoil knot and pentameric circular helicate assembly. *J. Am. Chem. Soc.* **141**, 3605–3612 (2019).
50. McConnell, A. J., Aitchison, C. M., Grommet, A. B. & Nitschke, J. R. Subcomponent exchange transforms an FeII4L4 cage from high- to low-spin, switching guest release in a two-cage system. *J. Am. Chem. Soc.* **139**, 6294–6297 (2017).
51. Kertesz, T. M., Hall, L. H., Hill, D. W. & Grant, D. F. CE_{50}: quantifying collision induced dissociation energy for small molecule characterization and identification. *J. Am. Soc. Mass. Spectrom.* **20**, 1759–1767 (2009).
52. Alexander, J. W. & Briggs, G. B. Annals of mathematics on types of knotted curves. *Second Ser.* **284**, 562–586 (1926).
53. Domoto, Y., Abe, M. & Fujita, M. A highly entangled (M3L2)8 truncated cube from the anion-controlled oligomerization of a π-coordinated M3L2 subunit. *J. Am. Chem. Soc.* **143**, 8578–8582 (2021).
54. Sørensen, A. et al. Chemical signals turn on guest binding through structural reconfiguration of triangular helicates. *Angew. Chem. Int. Ed.* **52**, 11273–11277 (2013).
55. Tarzia, A. Data for 'Assembly of a bifurcated knot via sequence selective imine condensation'. *Zenodo* https://doi.org/10.5281/zenodo.17589446 (2025).
56. Tarzia, A. andrewtarzia/sca_cage_assembler: submission of spindles. *Zenodo* https://doi.org/10.5281/zenodo.17999611 (2025).

Acknowledgements

We thank Diamond Light Source for synchrotron beamtime on I19 (CY21497 and CY29890).

Author contributions

J.T.F.D., J.A.D. and J.R.N. conceived of the study and wrote the paper. J.T.F.D. and J.A.D. performed the experiments and analysed the data.

T.K.R. collected the X-ray data and refined the crystal structure. A.T. and K.E.J. performed the computational calculations. X.S. synthesized subcomponent **C**. All authors discussed the results and commented on the paper.

Funding

J.T.F.D. thanks the Cambridge Trust (Vice Chancellor's and Trinity Hall Scholarship). J.R.N. thanks the European Research Council (ERC) (FunCapSys, ERC grant no. 695009). K.E.J. acknowledges the Royal Society for a University Research Fellowship and a Royal Society Enhancement Award 2018, and the ERC through grant agreement no. 758370 (ERC-StG-PE5-CoMMaD). A.T. acknowledges the funding received from the European Union under the NextGenerationEU programme (Mission 4 Component 1 CUP E13C22002930006). X.S. acknowledges the Deutsche Forschungsgemeinschaft (German Research Foundation, DFG) for a Walter Benjamin fellowship (grant no. SU-1426-1-1).

Competing interests

The authors declare no competing interests.

Additional information

Supplementary information The online version contains supplementary material available at https://doi.org/10.1038/s44160-026-01115-3.

Correspondence and requests for materials should be addressed to Jonathan R. Nitschke.

Peer review information *Nature Synthesis* thanks Guo-Xin Jin and the other, anonymous, reviewer(s) for their contribution to the peer review of this work. Primary Handling Editor: Bei Zhang, in collaboration with the *Nature Synthesis* team.

Reprints and permissions information is available at www.nature.com/reprints.

Publisher's note Springer Nature remains neutral with regard to jurisdictional claims in published maps and institutional affiliations.

Open Access This article is licensed under a Creative Commons Attribution 4.0 International License, which permits use, sharing, adaptation, distribution and reproduction in any medium or format, as long as you give appropriate credit to the original author(s) and the source, provide a link to the Creative Commons licence, and indicate if changes were made. The images or other third party material in this article are included in the article's Creative Commons licence, unless indicated otherwise in a credit line to the material. If material is not included in the article's Creative Commons licence and your intended use is not permitted by statutory regulation or exceeds the permitted use, you will need to obtain permission directly from the copyright holder. To view a copy of this licence, visit http://creativecommons.org/licenses/by/4.0/.

© The Author(s) 2026